

Low velocity impact response of 3D printed structures formed by cellular metamaterials and stiffening plates: PLA vs. PETg

F.A.Santos^a, H.Rebelo^b, M.Coutinho^c, L.S.Sutherland^d, C.Cismasiu^a, I.Farina^e, F.Fraternali^f

^aCERIS and Departamento de Engenharia Civil da Faculdade de Ciências e Tecnologia, Universidade NOVA de Lisboa, Quinta da Torre, 2829-516 Caparica, Portugal

^bCINAMIL and Departamento de Engenharia Civil da Faculdade de Ciências e Tecnologia, Universidade NOVA de Lisboa, Quinta da Torre, 2829-516 Caparica, Portugal

^cDepartamento de Engenharia Civil da Faculdade de Ciências e Tecnologia, Universidade NOVA de Lisboa, Quinta da Torre, 2829-516 Caparica, Portugal

^dCENTEC and Instituto Superior Técnico, Universidade de Lisboa, Lisboa 1049-001, Portugal

^eDepartment of Engineering, University of Naples “Parthenope”, 80143 Naples, Italy

^fDepartment of Civil Engineering, University of Salerno, 84084 Fisciano (SA), Italy

Abstract

This work studies the low-velocity impact response of 3D-printed layered structures made of thermoplastic materials (PLA and PETg), which form sacrificial claddings for impact protection. The analysed structures are composed of crushable cellular cores placed in between terminal stiffening plates. The cores tessellate either honeycomb hexagonal unit cells, or hexagonal cells with re-entrant corners, with the latter exhibiting auxetic response. The given results highlight that the examined PETg protectors exhibit higher energy dissipation ratios and lower restitution coefficients, as compared to PLA structures that have the same geometry. It is concluded that PETg qualifies as a useful material for the fabrication of effective impact protection gear through ordinary, low-cost 3D printers.

Keywords

Cellular metamaterials, Low velocity impact, PLA, PETg, Auxetic response

1. Introduction

Low-density materials capable of reducing the damage caused by shock due to impact loading are of great interest for protecting materials and structures [1], [2]. Architected materials that are receiving increasing interest are the so-called pentamode lattices, which shows very low shear moduli (theoretically equal to zero) [3], [4], [5], and may be able to stop or dramatically attenuate shear waves [5]. 2D versions of such lattices are offered by honeycomb

structures [6]. Also interesting are the kirigami lattices (origami and cuts/slits) that can easily switch on and off large negative or positive Poisson's ratios [7]. Auxetic response due to negative Poisson's ratios has shown to be able to offer marked resilience and energy dissipation capacity under impact loading [8], [9], [10], [11], [12].

The recent advances in additive manufacturing (AM) have paved the way to the rapid prototyping of lightweight sacrificial cladding for impact protection, whose fabrication would not be convenient via traditional, subtractive manufacturing techniques [13], [14], [15], [16], [17], [18], [19], [20], [21], [22]. Fused deposition modelling (FDM) is the most widespread AM technology, which can be handled by low-cost 3D printers. This technique resorts to a spool of thermoplastic filament to be melted and extruded through a heated nozzle and, subsequently, deposited in two-dimensional layers that will form a 3D printed object. A sacrificial cladding is usually composed of a crushable core placed in between two stiffening plates. The FDM technique makes it possible to customize easily the topology of the cellular core, and to optimize its structural performance in terms of a given figure of merit, which may involve, e.g., suitable stiffness, energy dissipation and/or resilience parameters. Several lattice geometries can be manufactured through FDM, which allows the easy fabrication of new and exciting metamaterials, with fascinating properties deriving from the internal architecture of the material [18]. Different lattice topologies have been considered to form sacrificial cladding in the literature, with particular focus on lattices based on different types of hexagonal unit cells [15]. As we already noticed, auxetic metamaterials have the capacity to sustain very high deformations under a constant low stress, mainly due to their compliant nature [8], [9], [15], [18]. Sacrificial cladding with honeycomb architecture, on the other hand, provide ultra-stiff structures which can accommodate large plastic damage while dissipating a significant amount of energy [20], [21]. As the mechanical performance of such metamaterials against impact loads mostly derives from the geometry of the cellular cores, many studies available in the literature to date have been focused on the shape optimization of the lattice geometry, rather than on the choice of the material [18], [19], [20], [21], [22]. Polylactic acid (PLA) is a thermoplastic polyester, which is cost-effective, widely diffused and easy to 3D print through consumer-level 3D printers. These reasons have led to the frequent use of PLA for the FDM of sacrificial cladding structures based on cellular metamaterials [13], [21]. However, much like other synthetic plastics, PLA has limited ability to absorb impact energy without failure [18], [21]. Due to their higher flexibility and good mechanical properties, polyethylene terephthalate glycol-modified (PETg) FDM filaments qualify as good candidates for the replacement of PLA in 3D printed protective gear [23], [24]. Some comprehensive studies on the failure mechanisms of a large variety of composite laminates and sandwich structures can be found in the following references [25], [26], [27], [28], [29], [30].

The main goal of this work is to study and compare the low-velocity impact response of PLA and PETg 3D-printed sacrificial cladding structures, which are manufactured through FDM. The analysed structures show honeycomb- and auxetic-type hexagonal unit cells. The manuscript is organized as follows. Section 2 illustrates the employed PLA and PETg materials, whose mechanical properties are characterized through tensile tests on dog-bone shaped specimens in Section 3. Section 4 presents a series of quasi-static indentation tests on PLA and PETg sacrificial claddings with different internal architectures. Low-velocity impact tests on PLA and PETg protectors are given in Section 5, using a fully instrumented falling weight machine.

2. Materials

All of the protectors analysed in this work were manufactured by processing a single spool of commercial PLA and PETg filaments with 1.75 mm diameter, using a Prusa i3 MK2 3D printer with a 0.4 mm diameter nozzle [31]. The examined cellular topologies make use of the hexagonal cell geometry represented in Figure 1. By setting the parameters and, shown in Figure 1, to the values presented in Table 1, we obtained the honeycomb and auxetic–hexagonal cellular geometries with re-entrant corners depicted in Figure 2(a) and (b), respectively. In order to obtain the same relative density of 25% for both specimens, we adjusted the thickness of the corresponding cells accordingly, by prescribing a thickness of 1.0 mm for the honeycomb geometry and a thickness of 0.8 mm for the auxetic geometry. We were able to obtain layered structures with approximately the same mass (240 g and 230 g for the honeycomb and auxetic–hexagonal, respectively). Such a key result substantiates the energy absorption comparisons presented throughout the paper. The sacrificial cladding specimens consisted of 100 x 100 x 50 mm³ blocks comprising the cellular, crushable, cores sandwiched between two 5 mm stiffening plates (cf. Figs. 3 and 4). The printing parameters used to fabricate all the 3D-printed specimens analysed in the present study are listed in Table 2.

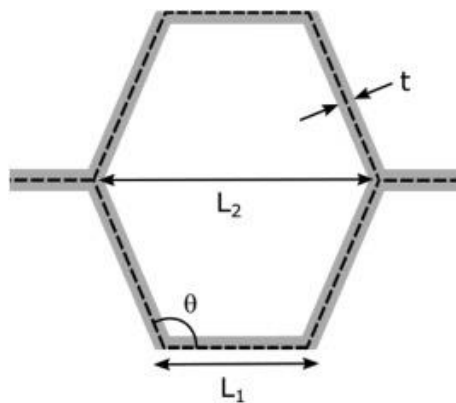
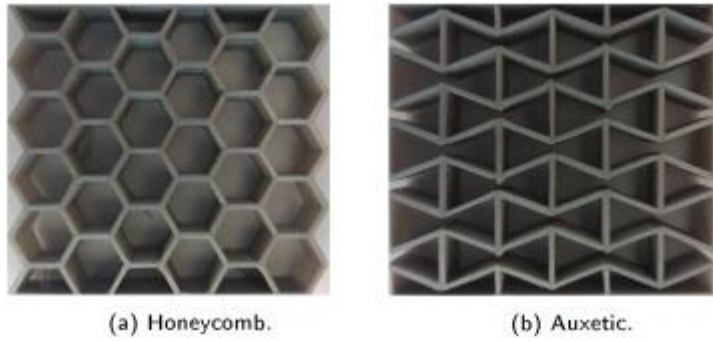


Figure 1. Layout of the hexagonal cell.

	L_1	L_2	ϑ	t
	(mm)	(mm)	(degrees)	(mm)
Honeycomb	5	10	120	1
Auxetic	5	1.5	70	0.8

Table 1. Geometric parameters of the employed hexagonal cell.



(a) Honeycomb.

(b) Auxetic.

Figure 2. Structures of the cellular cores.

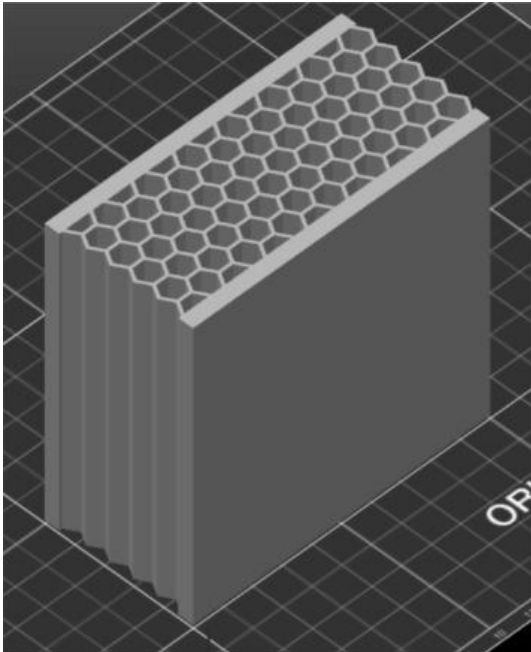


Figure 3. Honeycomb sacrificial cladding.

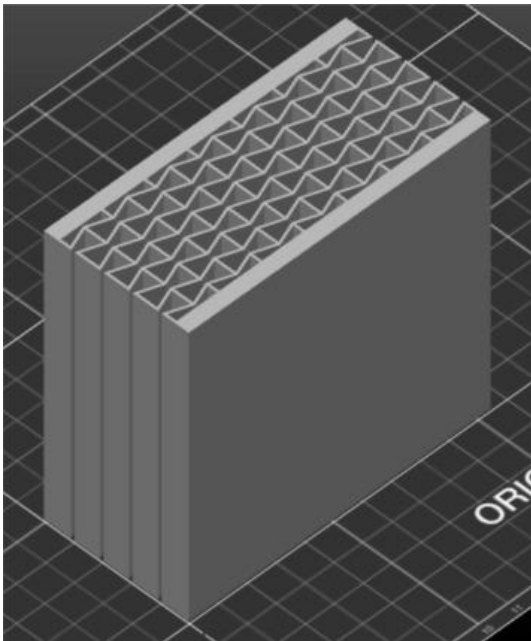


Figure 4. Auxetic sacrificial cladding.

	PLA	PETg
Nozzle extrusion temperature	210 °C	250 °C
Heated bed temperature	60 °C	50 °C
Layer height	0.2 mm	0.2 mm
Printing speed	30 mm/s	30 mm/s
Number of outer shells	2	2

Table 2. 3D printing parameters.

3. Uniaxial tensile tests

The ASTM D638 Standard Test Methods for Tensile Properties of Plastics [32] was used to characterize the mechanical properties of the employed PLA and PETg materials. Three standard, dog-bone shaped specimens (Type IV) for each material were 3D printed and tested. The specimens were printed with 100% infill and a raster orientation of 45 degrees (see Figure 5). Due to the layered microstructure resulting from the FDM process, some damage due to non-perfect interlayer adhesion is to be expected in the 3D printed specimens. A raster orientation of 45 degrees was employed to mitigate such an issue [33]. The thickness and width of each specimen were measured at several different locations. Table 3 provides information about the mass and the geometry of the each 3D-printed specimen subjected to tensile tests (refer to Figure 1 for the notation).

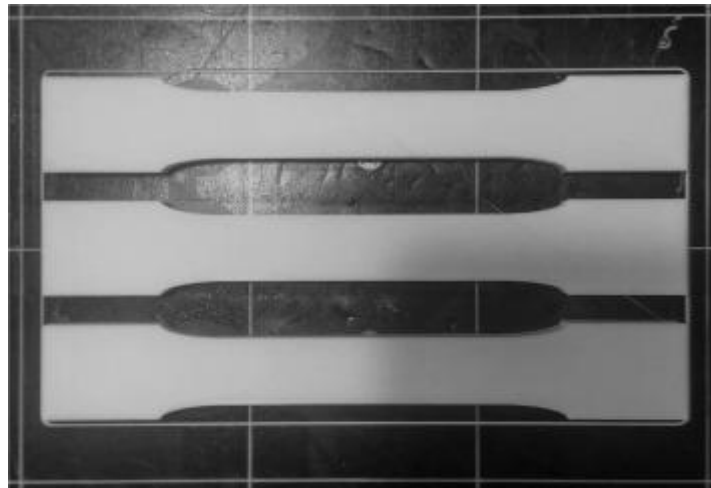


Figure 5. 3d-printed dog-bone specimens.

The tensile tests were performed on a Zwick/Roell Z50 universal machine, with a strain-rate of 0.1%/s, using a gauge length of 50 mm for strain analysis, as shown in Figure 6. Figure 7 illustrates the force vs. displacement curves obtained during the tensile tests for PLA and PETg specimens, while Table 4 lists the key results of such tests in terms of yield stress σ_y , ultimate stress σ_u , yield strain ϵ_y , ultimate (break) strain ϵ_u , and Young modulus E .

	M	L₁	L₂
	(g)	(mm)	(mm)
PLA 1	15.81	14.22	6.35
PLA 2	15.84	14.09	6.41
PLA 3	15.80	14.20	6.42
PETg 1	16.51	14.01	6.09
PETg 2	16.16	14.07	6.17
PETg 3	16.17	13.87	6.18

Table 3. Material and geometric properties of the specimens subjected to tensile tests.



Figure 6. Illustration of the tensile testing procedure.

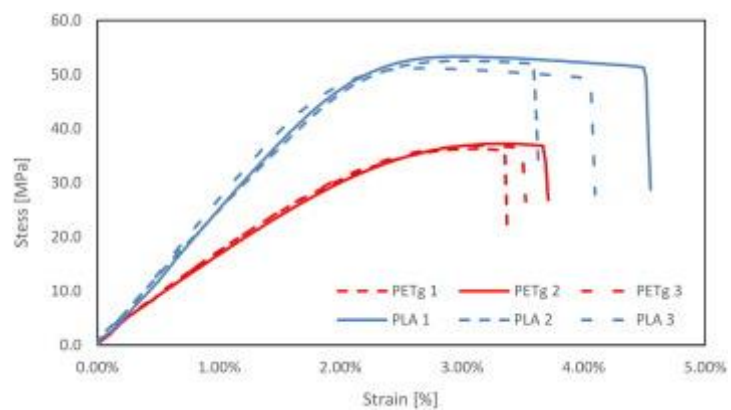


Figure 7. Force–displacement diagrams of tensile tests.

	σ_y	σ_u	ϵ_y	ϵ_u	E
	(MPa)	(MPa)	%	%	(GPa)
PLA 1	53.1	51.3	2.31	4.51	2.77
PLA 2	52.2	50.1	2.36	3.63	2.75
PLA 3	51.0	49.3	2.55	3.71	2.74
PETg 1	34.01	36.8	2.31	3.67	1.81
PETg 2	34.10	37.2	2.33	3.37	1.80
PETg 3	34.45	36.5	2.29	3.48	1.82
PLA (avg)	52.10	50.23	2.41	3.95	2.75
PLA (sd)	1.05	1.01	0.13	0.49	0.02
PETg (avg)	34.19	36.83	2.31	3.51	1.81
PETg (sd)	0.23	0.35	0.02	0.15	0.01

Table 4. Results of tensile tests.

The results presented in Figure 7 and Table 4 show that the Young modulus and the tensile toughness of the PLA specimens (i.e., the area underneath the stress–strain curve) are higher than those exhibited by the PETg samples. It is worth noting that other studies available in literature indicate different results in terms of the energy absorption capacities of these materials, and a greater toughness of PETg over PLA [23], [34]. Such different findings are explained by the fact that the mechanical properties of FDM parts may vary significantly from those of the bulk materials, since they markedly depend on the 3D printing process and the employed settings. We wish to remark, however, that the results presented in the subsequent sections highlight rather good impact protection performances of the PETG structures analysed in this study. The tensile tests helped us to establish a general framework for this study. They provided an important insight into the main mechanical properties of 3D printed specimens obtained by FDM, and helped us to establish the main differences in the constitutive behaviour shown by PLA and PETg samples. These results will also be very useful in future studies aimed at the numerical modelling of the analysed cellular metamaterials.

4. Quasi-static indentation tests

Quasi-static (QS) indentation tests were carried out on an instrumented servo–hydraulic test machine at a constant displacement rate, by using a hemispherical ended cylindrical indentation head with 30 mm diameter (see Figure 8) [35], [36], aligned with the centre of

the tested specimens. The specimens were simply supported on a steel apparatus with an outside diameter of 100 mm and a central circular hole featuring 50 mm diameter. We examined one specimen for each analysed topology and material.



Figure 8. Servo-hydraulic test machine.

Let us begin by presenting the results of QS tests on honeycomb sacrificial cladding specimens (Figure 9, Figure 10). Figure 11, Figure 12 illustrate the force vs. displacement, and the absorbed energy vs. displacement plots obtained for such specimens, respectively. The absorbed energy refers to the area under the force vs. displacement curve up to the current value of the displacement at the indentation point.

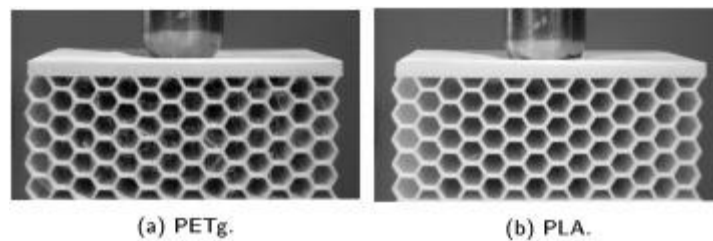


Figure 9. PETg and PLA honeycomb specimens subjected to QS tests.

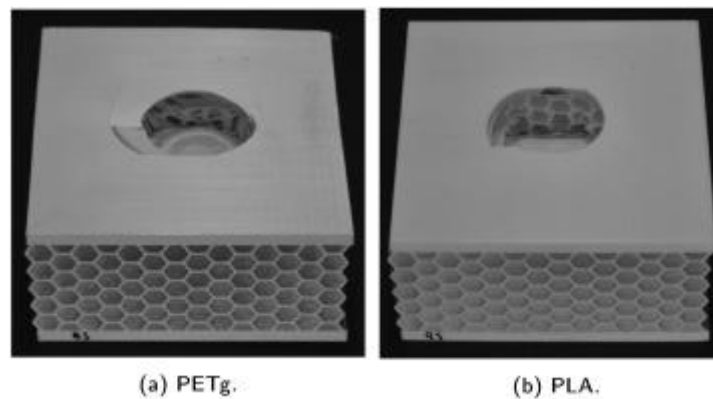


Figure 10. Failure patterns of damaged PETg and PLA honeycomb specimens subjected to QS tests.

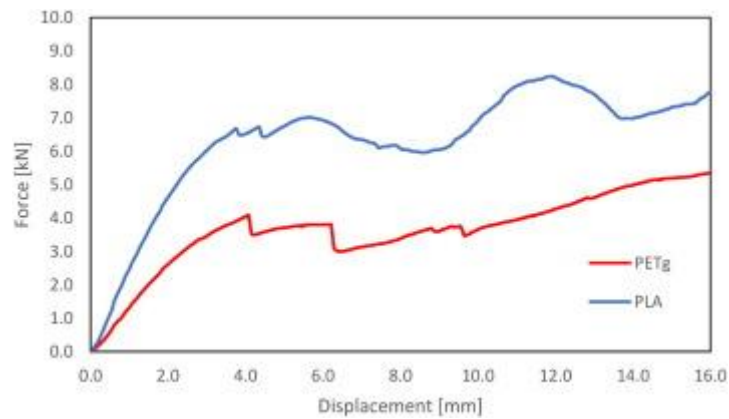


Figure 11. Force–displacement response of the honeycomb specimens subject to QS test.

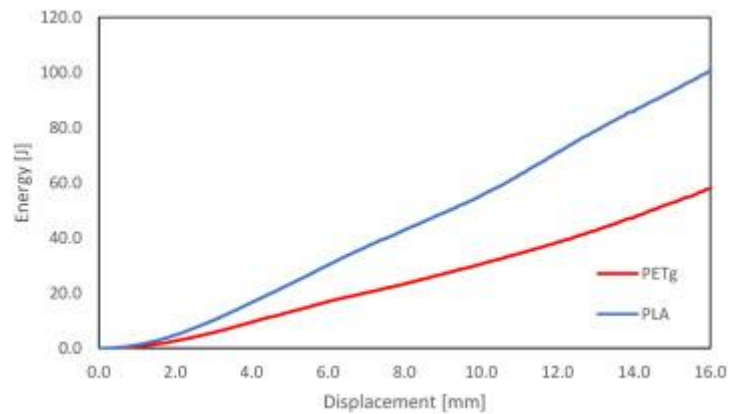


Figure 12. Absorbed energy-displacement of the honeycomb specimens subject to QS test.

The visual observation of the deformation patterns exhibited by the examined protectors under QS tests highlighted the occurrence of the highest strain concentrations in the proximity of the indentation head, and similar failure mechanisms for both PLA and PETg specimens. Figure 11 highlights that the first peak of the indentation force (attained before the densification of the specimen occurs) corresponds to a vertical displacement of the indenter head of about 4 mm, both for the PLA and the PETg specimens. The PETg structure showed larger displacements, as compared to the PLA sample, and a first peak force of about 4.0 kN. The PLA protector instead suffered a first peak force of 6.5 kN, and showed energy absorption capacity higher than the PETg structure (Figure 12).

Passing to examine the response of auxetic sacrificial claddings to QS tests, we refer the reader to Figures 13 and 14, which illustrate the configurations of the PETg and PLA specimens at the end of the tests. The auxetic behaviour of the specimens with re-entrant corners is clearly visible, being associated with the displacement of the core material towards the centreline. Regarding the failure pattern exhibited by the auxetic specimens, we observe the occurrence of fracture lines in the top plate that run perpendicularly to the edges of the protector. The width of the fracture lines is larger than the indenter head. We also observe that PETg specimens show a more pronounced damage than do PLA specimens. Such a distributed failure pattern markedly differs from the localized damage observed in the honeycomb specimens.

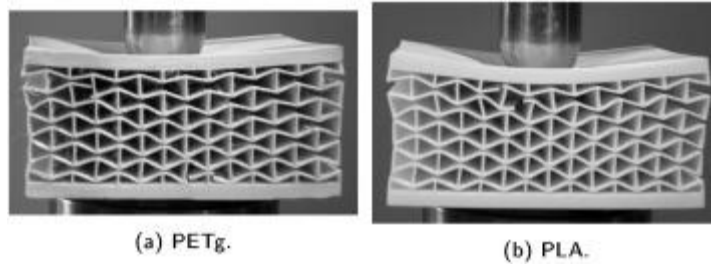


Figure 13. PETg and PLA auxetic specimens under the first peak load of QS tests.

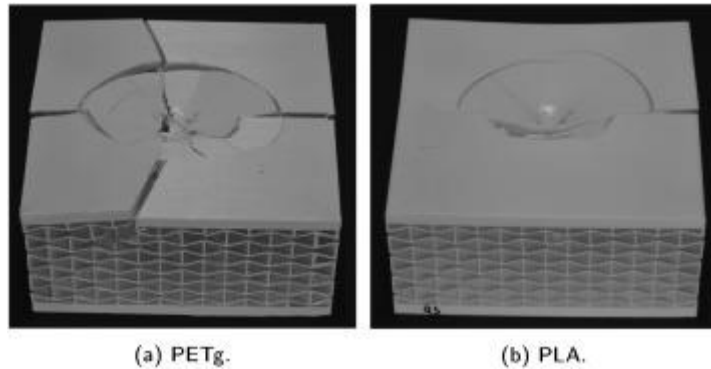


Figure 14. Failure patterns of damaged PETg and PLA auxetic specimens under QS tests.

Figures 15 and 16 depict the force vs. displacement and the absorbed energy vs. displacement curves of the auxetic specimens, respectively.

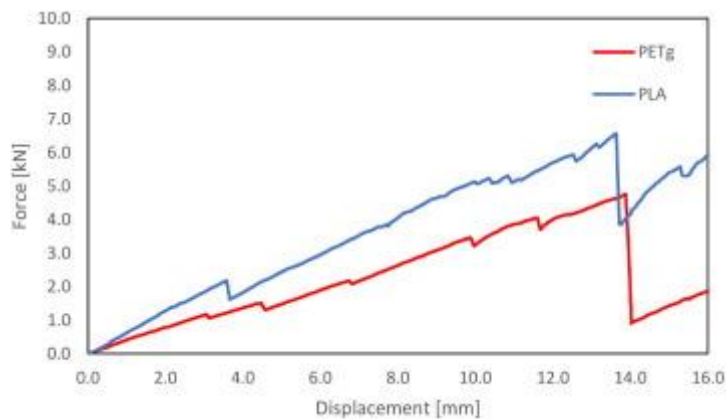


Figure 15. Force–displacement response of auxetic specimens under QS test.

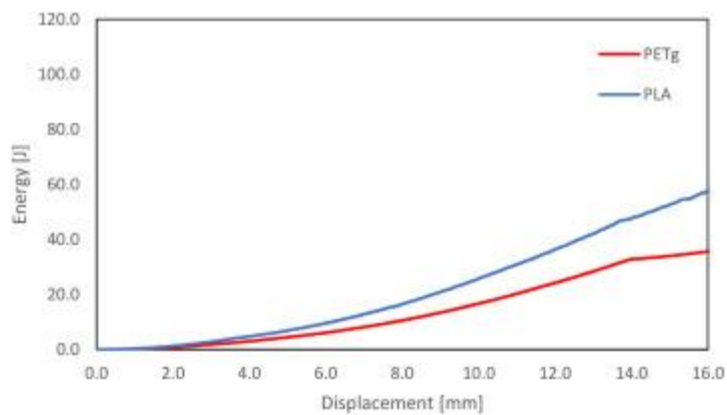


Figure 16. Absorbed energy-displacement curves of auxetic specimens under QS test.

Both the PLA and the PETg auxetic samples showed a remarkable capacity to accommodate large and recoverable displacements under quasi-static loading, which is demonstrated by

the attainment of a displacement of 14 mm under the first peak load. Such a displacement is 3.5 times higher than the corresponding displacements exhibited by the honeycomb specimens (Figure 11). The PLA auxetic structure exhibited a stiffer response, over the PLA protector, and reached a first peak force of 6.5 kN, against a first peak force of 4.0 kN of the auxetic PETg structure. One observes that such force values are quite similar to those obtained for the honeycomb specimens (cf. Figure 15, Figure 11). In terms of absorbed energy, the PLA auxetic protector was able to absorb about 30 % more energy than the PETg auxetic structure, during the elastic phase of force vs. displacement response.

We were able to employ the QS tests also to estimate the Poisson's ratios of the honeycomb and auxetic claddings. Such a result was obtained by tracking the vertical and horizontal displacements of the lattice cores, via digital image processing (DIP) techniques, in correspondence with the linear branch of the force–displacement responses. The Poisson's coefficients were estimated by computing the ratio between the lateral and vertical strains of the lattices. Table 5 shows the computed values of such effective Poisson's ratios for the PLA protectors, which amount to 0.19 and –0.38 for the honeycomb and auxetic structures, respectively. Very similar results were obtained for the PETg protectors.

	Hexagonal	Auxetic
Vertical deformation [%]	2.56	3.12
Horizontal deformation [%]	0.48	–1.18
Poisson coefficient	0.19	–0.38

Table 5. Poisson's ratios of the PLA structures subjected to QS tests

5. Low-velocity dynamic tests

Low-velocity impact tests were performed using a fully instrumented Rosand IFW5 falling weight machine (Figure 17 [36]). We employed the same cylindrical impact head with hemispherical cap used for the QS tests, which now was dropped from a given height between guide rails onto the horizontally supported 3D printed sample. A large mass was attached to the impact head and a load cell was employed to measure the variation of the impact force with time. The measured data was post-filtered to remove noise from the recorded signal. An optical gate measured the incident velocity of the impactor head. The time-histories of the displacement of the impactor head and the absorbed energy were calculated through numerical integration of the measured velocity–time and force–time data, respectively. A Photron Fastcam Mini Ax high-speed camera (HSC) was used at a frame rate of 10,000 frames per second and a resolution of 768 by 528 pixel. All the measurements were synchronized using a light intensity trigger. The test parameters were tuned to apply two different levels of incident kinetic energy on the examined honeycomb and auxetic structures (10 and 20 J).



Figure 17. Rosand IFW5 instrumented falling weight impact tester.

Figures 18 to 21 illustrate the results obtained for the low-velocity impact tests on honeycomb structures subjected to an incident kinetic energy of 10 J. Several frames extracted from the recordings of such impact tests are shown in Figure 18 (a)–(d). Here, and denote the times associated with the maximum force and the maximum displacement before rebound, respectively. The results illustrated in the above figures and also in Figure 18 (e) and (f), with the corresponding failure patterns, highlight that all the examined honeycomb structures suffered limited deformation under the 10 J impact loading, and that the PLA specimens showed negligible fracture damage. The force–displacement plot in Figure 19 highlight that the PLA specimen exhibits a maximum displacement of 3.2 mm with no residual deformation after impact. The maximum force transmitted to the PLA specimen was nearly equal to 6.0 kN. The PETg specimen instead suffered some limited permanent damage (observe the nonzero residual displacement under zero force in the plot of Figure 19), a maximum displacement of 5.6 mm, and a transmitted force of 3.2 kN.

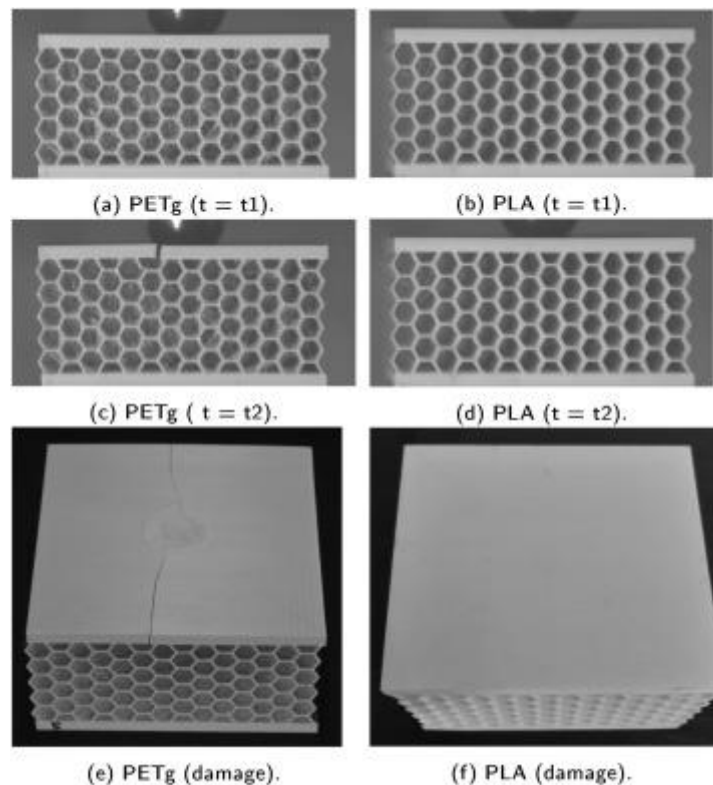


Figure 18. Frames from 10 J impact tests on honeycomb structures.

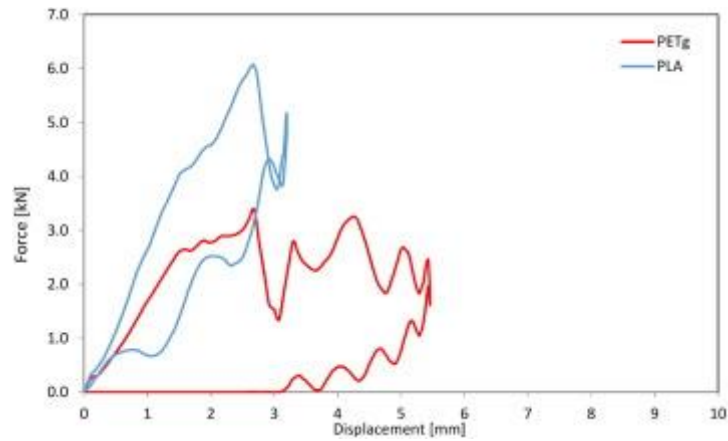


Figure 19. Force–displacement responses of honeycomb structures under 10 J impact loading.

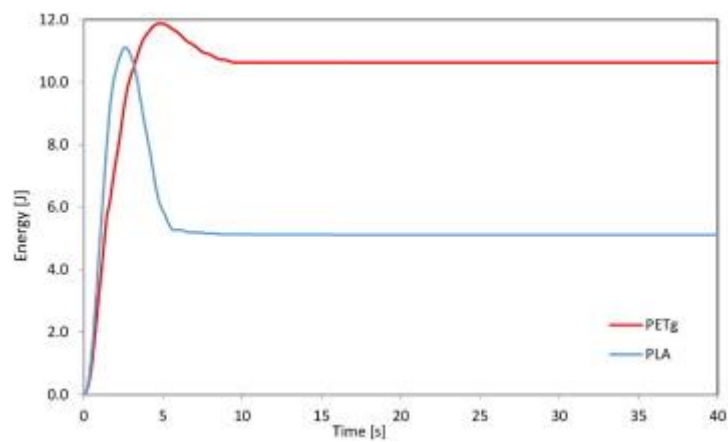


Figure 20. Energy time-histories of honeycomb structures under 10 J impact loading.

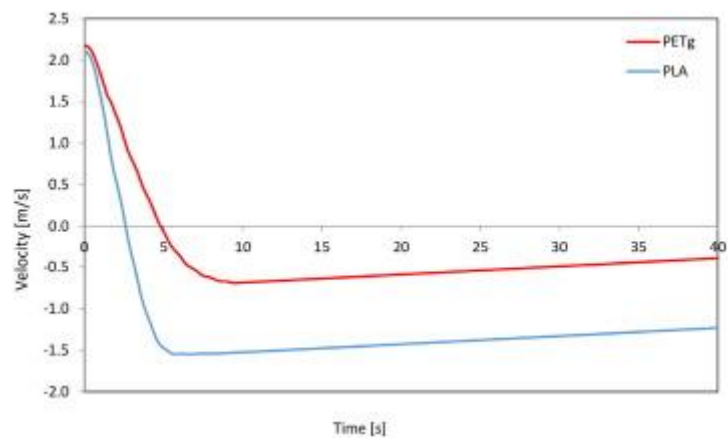


Figure 21. Velocity time-histories of honeycomb structures under 10 J impact loading.

Figure 20 illustrates the responses of the honeycomb structures in terms of absorbed and dissipated energies. While one observes that the absorbed energy is similar for PLA and PETg honeycomb protectors, the amount of dissipated energy (i.e., the value of the horizontal plateau in right-hand side of the graph) is quite different in such systems. The PETg cladding indeed dissipates almost 90% of the absorbed energy (i.e., it exhibits a 90% energy dissipation factor factor), while the PLA cladding dissipates only 45% of the impact energy. Figure 21 shows the velocity response of the impactor head during the current tests, highlighting that the PETg protector exhibits significantly lower impact velocities than the PLA protector. Let us define the restitution coefficient of the impacted structure as $|v_{out}|/|v_{in}|$, with v_{in} being

the velocity at the time of impact, and v_{out} being the rebound velocity of the impactor head. Our calculations show that the restitution coefficients of the PLA and PETg claddings are respectively equal to 74% and 32%. Overall, we conclude that the PETg honeycomb structure dissipates more impact energy than the PLA honeycomb protector, and produces, at the same time, a smaller rebound velocity of the impactor.

The results of the 10 J impact tests on auxetic sacrificial claddings are illustrated in Figure 22, Figure 23, Figure 24, Figure 25. The analysis of the results shown in such figures leads us to observe that both PLA and PETg auxetic structures suffered more marked damage and larger displacements, as compared to the honeycomb structures (cf. Figure 18, Figure 22). The general trends of the impact responses of the auxetic structures are quite similar to those observed in the honeycomb structures under the same loading condition, as one realizes by comparing Figures 18 to 21 with Figures 22 to 25. The force–displacement curves depicted in Figure 23 show that the PLA auxetic structure exhibits a maximum displacement of 7.5 mm, and a maximum force of 2.3 kN. The PETg auxetic structure instead shows a maximum displacement of 9.7 mm, and a transmitted force of only 1.8 kN. The performances of the auxetic sacrificial claddings in terms of absorbed and dissipated energies are illustrated by the plots in Figure 24. Such a figure highlights that the PETg cladding exhibits a high-energy dissipation ratio, which is equal to 83%, while the PLA cladding dissipates 71% of the impact energy. Figure 25 illustrates the velocity responses of the impactor head during 10 J dynamic tests on the auxetic structures. One observes from the results in such a figure that the PETg protector produces lower rebound velocities than the PLA specimen. The restitution coefficients for the PLA and PETg auxetic structures are respectively equal to 53% and 40%.

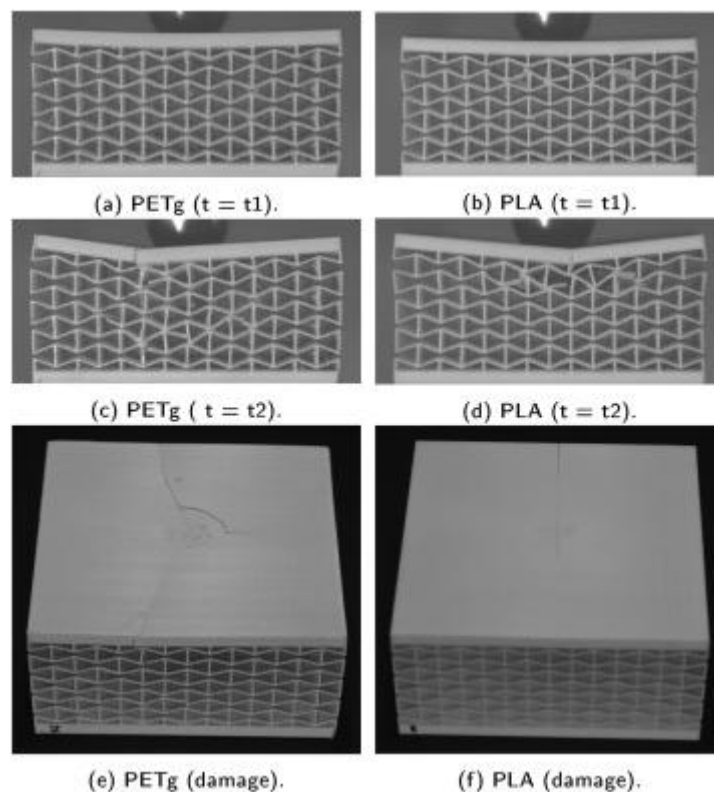


Figure 22. Frames extracted from the 10 J impact tests on auxetic structures.

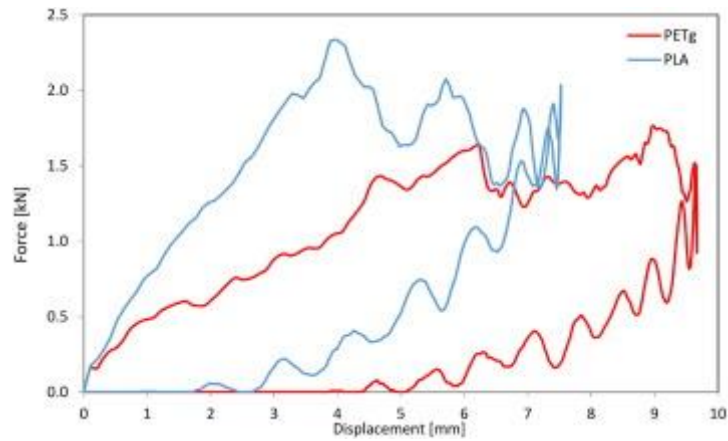


Figure 23. Force–displacement responses of auxetic structures under 10 J impact loading.

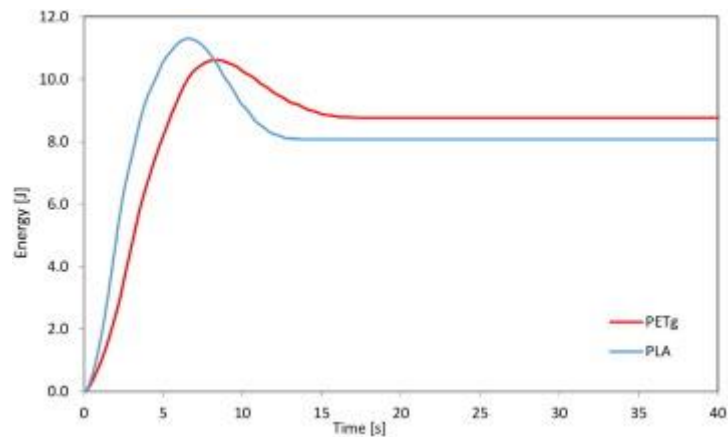


Figure 24. Energy time-histories of auxetic structures under 10 J impact loading.

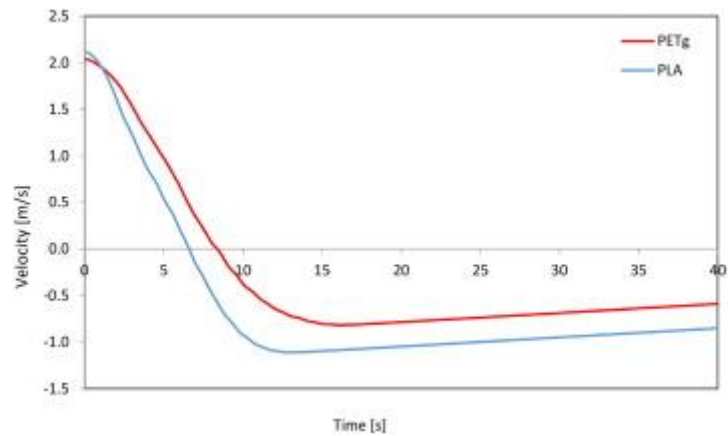


Figure 25. Velocity time-histories of auxetic structures under 10 J impact loading.

We close the present section by illustrating the results of impact tests on honeycomb and auxetic sacrificial claddings subjected to impact loading with 20 J incident kinetic energy (Figures 26 to 33). An analysis of these results reveals that the current loading condition produces noticeable damage of all the examined structures, which becomes particularly relevant in the case of the auxetic claddings (see Figure 30). It is easy to verify that the increased fracture damage of the specimens subject to 20 J impact loading, as compared to the structures undergoing 10 J impact loading, translates into higher energy dissipation ratios and lower restitution coefficients.

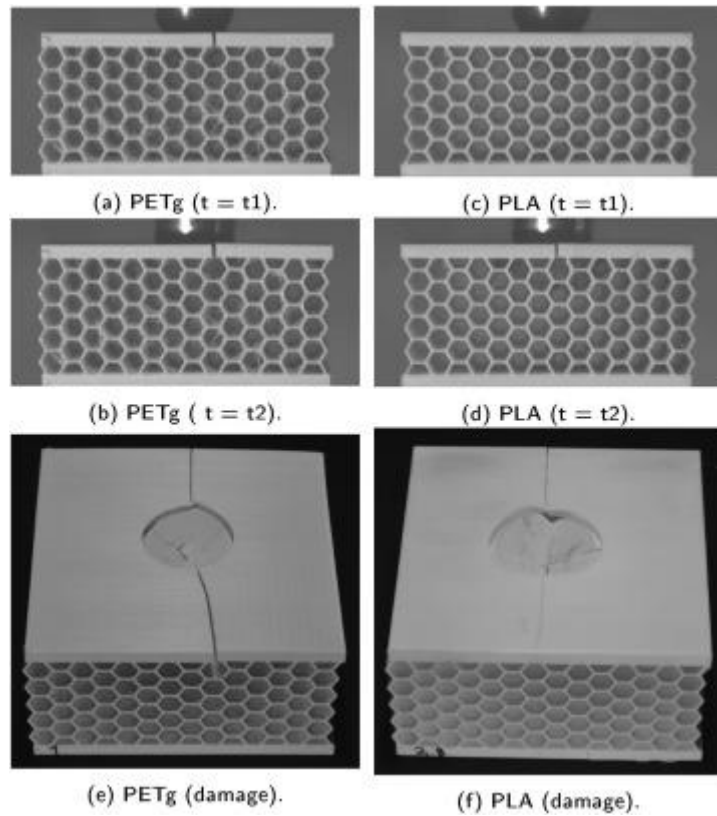


Figure 26. Frames extracted from the 20 J impact tests on honeycomb structures.

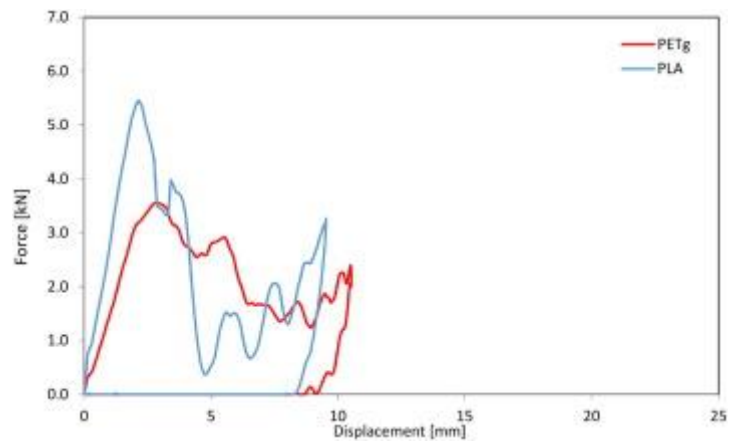


Figure 27. Force–displacement responses of honeycomb structures under 20 J impact loading.

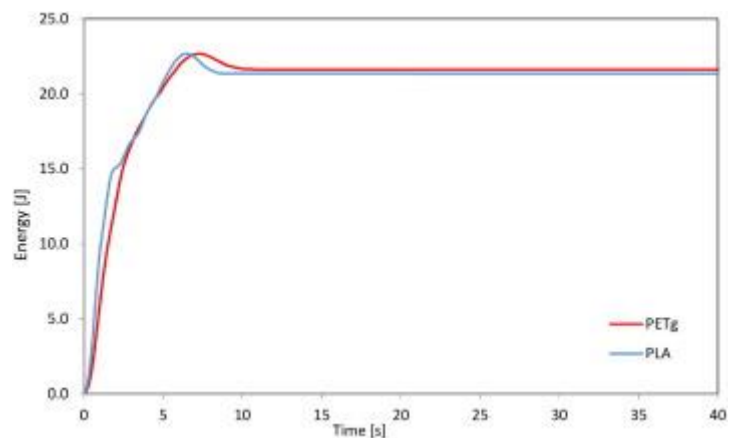


Figure 28. Energy time-histories of honeycomb structures under 20 J impact loading.

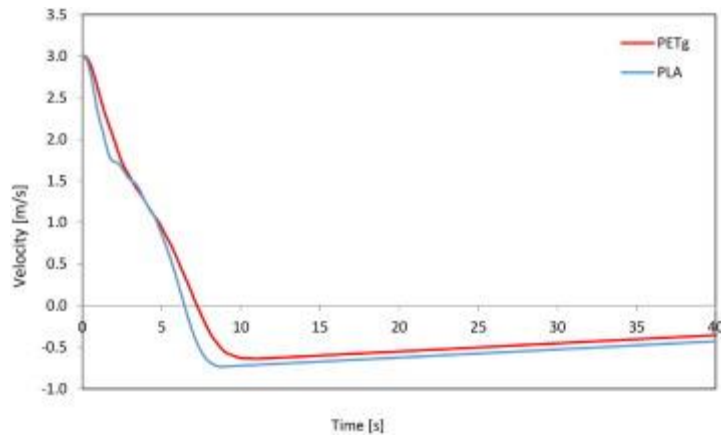


Figure 29. Velocity time-histories of honeycomb structures under 20 J impact loading.

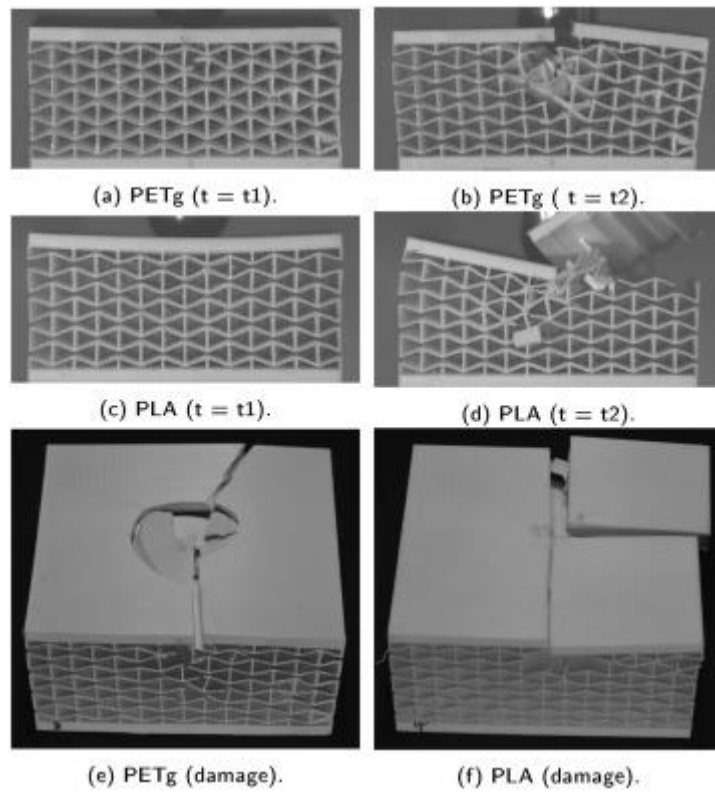


Figure 30. Frames extracted from the 20 J impact tests on auxetic structures.

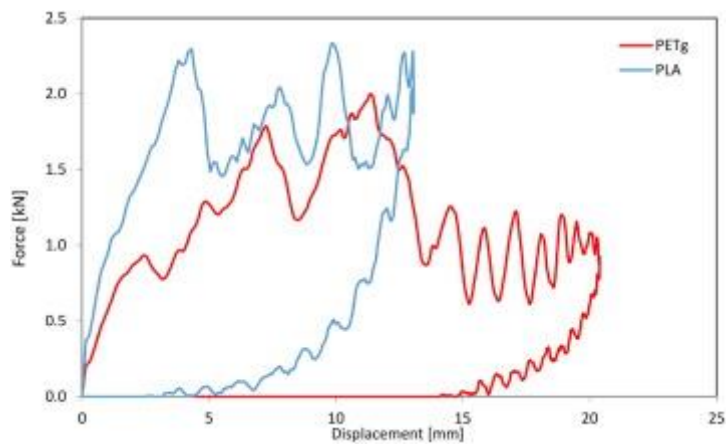


Figure 31. Force-displacement responses of auxetic structures under 20 J impact loading.

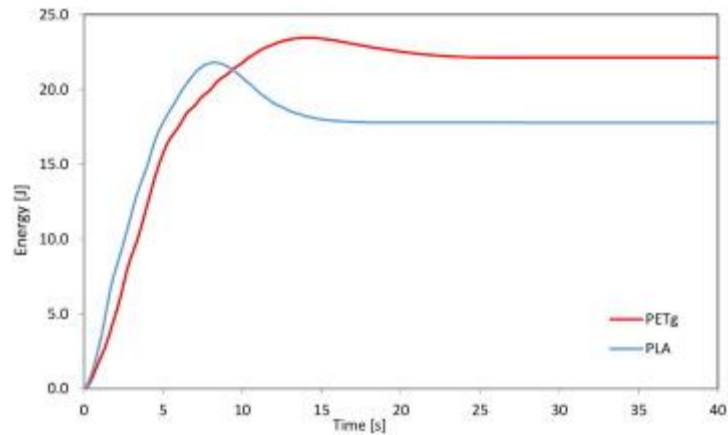


Figure 32. Energy time-histories of auxetic structures under 20 J impact loading.

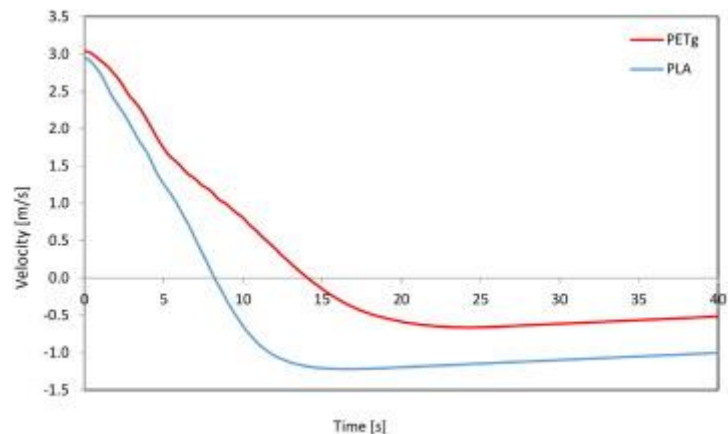


Figure 33. Velocity time-histories of auxetic structures under 20 J impact loading.

6. Discussion

The results presented in the previous section have highlighted that the examined PETg structures exhibit superior impact protection ability over the PLA protectors, due to higher energy dissipation factors and lower restitution coefficients. The higher compliance of the PETg protectors produces higher strains and smaller transmitted forces in these structures under impact loading, always comparing with the PLA protectors. The combination of such effects leads us to recognize the superior performance of PETg protectors over the PLA counterparts, and paves the way to the AM of effective PETg impact protection gear through ordinary 3D printers.

An important question to address is whether the results of quasi-static tests can be employed to predict the dynamic response of sacrificial claddings. Figure 34, Figure 35, Figure 36, Figure 37 show a prediction of the maximum forces and displacements that can be estimated by processing the results of QS tests for the various structures under examination, in correspondence with both 10 J and 20 J energy inputs. Such predictions were computed by measuring the area under the force vs. displacement curves of the QS tests, as it is shown in Figures 34 to 37.

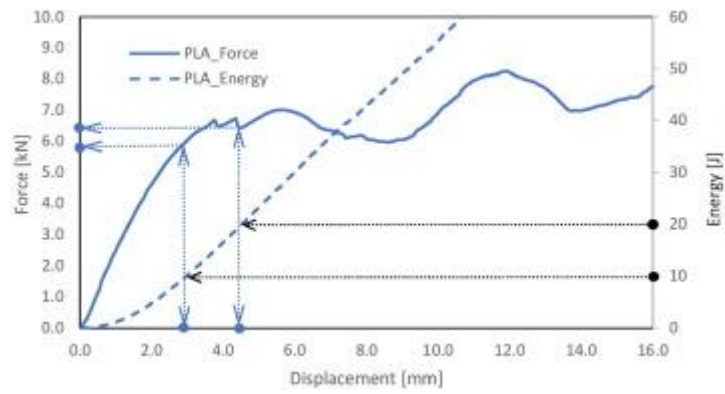


Figure 34. Force and displacement estimates from QS tests (PLA-honeycomb).

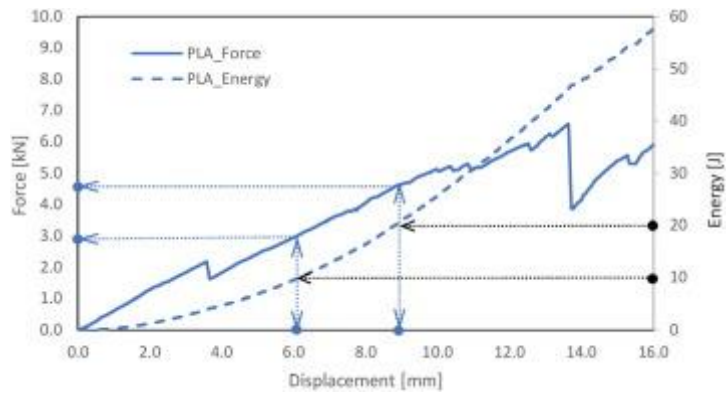


Figure 35. Force and displacement estimates from QS tests (PLA-auxetic).

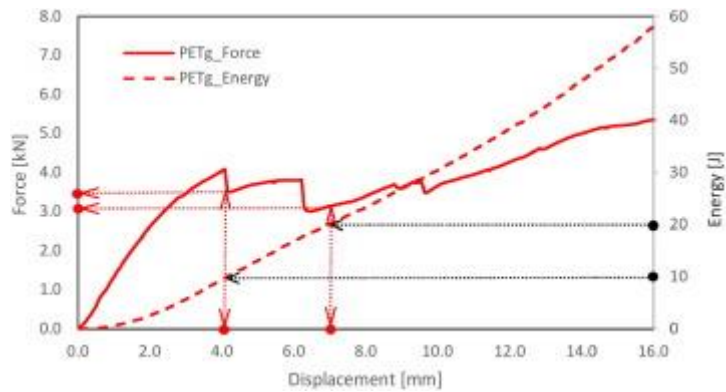


Figure 36. Force and displacement estimates from QS tests (PETg-honeycomb).

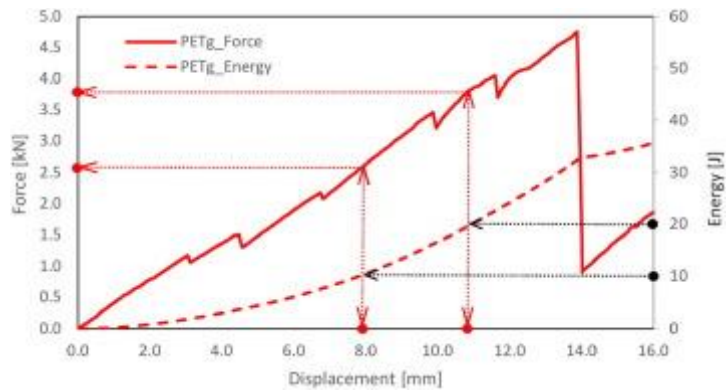


Figure 37. Force and displacement estimates from QS tests (PETg-auxetic).

An overview of the results of the QS and low-velocity dynamic tests examined in this paper is offered by the bar diagrams depicted in Figures 38 to 41. With reference to the honeycomb

protectors, the bar diagram in Figure 38 highlights that QS tests provide reasonably good estimates of the maximum force that is transmitted by the cladding. For auxetic structures, the QS tests still yield a good estimate of the transmitted force in the case of the 10 J loading condition, while for the 20 J case the QS estimate of the maximum force is rather lower than the dynamically observed value. Figure 39 shows a comparison between the predictions of the maximum displacements exhibited by the examined protectors. One notices that the QS tests provide reasonable good estimates of the maximum displacement exhibited by the honeycomb and auxetic structures in correspondence with the 10 J energy impact loading condition, and very rough estimates in the 20 J case. It is worth observing that the displacements predicted through QS tests are always lower than those experimentally observed under dynamic loading. Figures 40 and 41 provide bar diagrams of the energy dissipation ratios and the restitution coefficients exhibited by all the examined protectors. Such diagrams confirm that the PETg protectors exhibit higher dissipated energy ratios and lower restitution coefficients over the PLA samples, as we already observed.

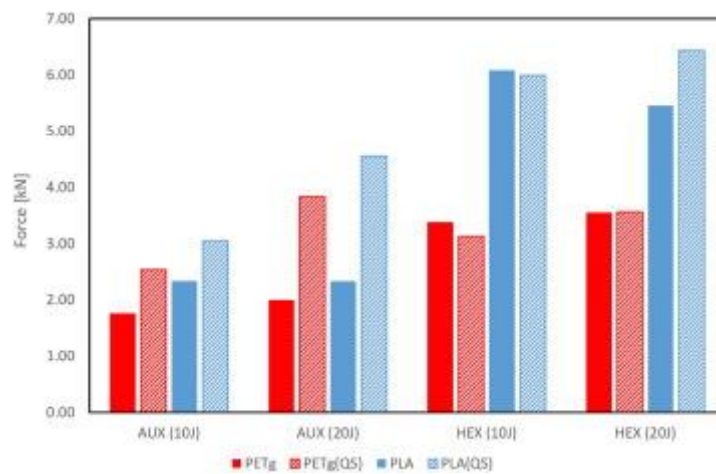


Figure 38. Bar diagrams of the maximum forces recorded in the impact tests.

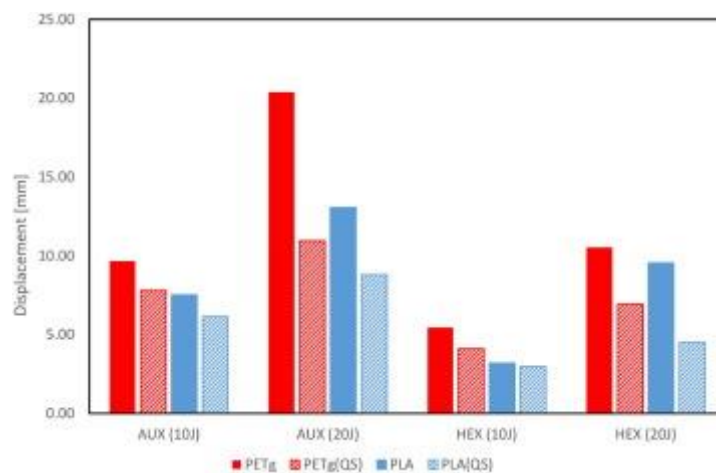


Figure 39. Bar diagrams of the maximum displacements recorded in the impact tests.

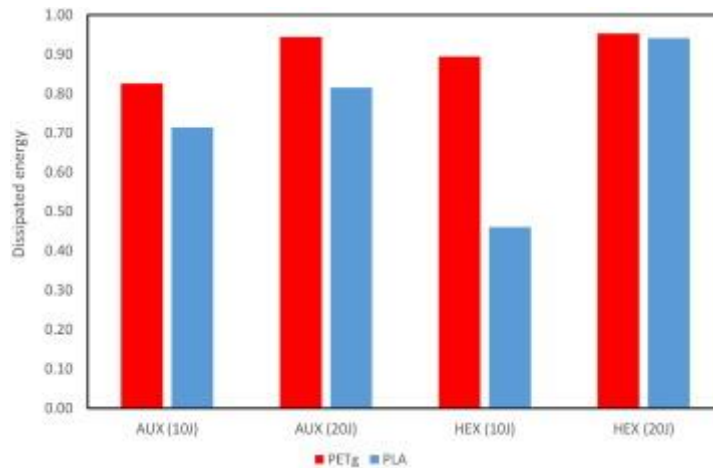


Figure 40. Bar diagrams of the dissipated energy ratios.

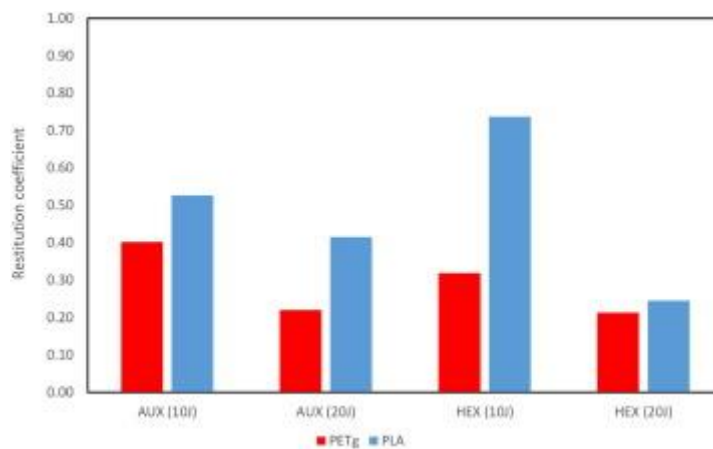


Figure 41. Bar diagrams of the restitution coefficients.

The damage patterns shown by the specimens during the quasi-static tests were quite similar to the ones observed during the low-velocity dynamic tests, for both the tested geometries and materials. The protectors with auxetic geometry proved to be able to mobilize a significant higher volume of material during the impact tests. Such protectors exhibited more extensive cracking patterns and higher energy dissipation, as compared to honeycomb protectors.

7. Concluding remarks

This paper has experimentally studied the low-velocity impact response of 3D-printed sacrificial claddings, which have been manufactured by processing PLA and PETg filaments for FDM, through an ordinary 3D printer. The results presented throughout this study allow us to draw the following main conclusions:

1. PETg sacrificial claddings show higher energy dissipation ratios and lower restitution coefficients over the examined PLA protectors.
2. The higher flexibility of PETg protectors induces larger impact strains in such structures, as compared to PLA structures with same geometry, but reduces the amplitude of the transmitted force.
3. Under low energy impact loading, QS tests can provide good estimates of the maximum force transmitted by the protector.

We plan to enrich the research presented in this study by conducting future work on the high velocity impact response of the examined protectors. Such a study will be aimed at extending the present comparison between the performances of PETg and PLA sacrificial claddings in the high-energy regime. Additional future research lines will be devoted to the design of novel impact protection gear to be manufactured with AM materials on a variety of 3D printers at different scales. The final goal of this research will be a proof-of-principle of the current project concepts and methodology through the additive manufacturing of a full-scale helmet prototype featuring enhanced mitigation of traumatic brain injury and concussion [37]. The impact-absorbing liner of such a helmet will be aimed at reproducing the skull-brain system, with the outer section mimicking the skull, through a pressure-wave mitigation lattice, and the inner section mimicking the cerebrospinal fluid via a shear-wave mitigation or ‘metafluid’ lattice [4].

Acknowledgements

F.F. acknowledges financial support from MIUR under the PRIN 2017 National Grant ‘Multiscale Innovative Materials and Structures’(Grant No. 2017J4EAYB).

F.S. acknowledges the support from the Centro de Competências para a Proteção de Infraestruturas (CCPI) of the Military Academy, during the experimental tests.

References

- [1] T.A. Schaedler, C.J. Ro, A.E. Sorensen, Z. Eckel, S.S. Yang, W.B. Carter, A.J. Jacobsen
Designing metallic microlattices for energy absorber applications
Adv Eng Mater, 16 (3) (2014), pp. 276-283, 10.1002/adem.201300206
- [2] F. Fraternali, M.A. Porter, C. Daraio
Optimal design of composite granular protectors
Mech Adv Mater Struct, 17 (1) (2009), pp. 1-19, 10.1080/15376490802710779
- [3] R. Schittny, T. Bückmann, M. Kadic, M. Wegener
Elastic measurements on macroscopic three-dimensional pentamode metamaterials
Appl Phys Lett, 103 (23) (2013), Article 231905, 10.1063/1.4838663
- [4] A. Amendola, C.J. Smith, R. Goodall, F. Auricchio, L. Feo, G. Benzoni, F. Fraternali
Experimental response of additively manufactured metallic pentamode materials confined between stiffening plates
Compos Struct, 142 (2016), pp. 254-262, 10.1016/j.compstruct.2016.01.091
- [5] A. Martin, M. Kadic, R. Schittny, T. Bückmann, M. Wegener
Phonon band structures of three-dimensional pentamode metamaterials
Phys Rev B, 86 (15) (2012), Article 155116, 10.1103/PhysRevB.86.155116
- [6] A.N. Norris
Mechanics of elastic networks
Proc R Soc A, 470 (2014), p. 20140522, 10.1098/rspa.2014.0522
- [7] R.M. Neville, F. Scarpa, A. Pirrera
Shape morphing Kirigami mechanical metamaterials

Scientific Reports, 6 (2016), Article 31067, 10.1038/srep31067

- [8] F. Scarpa, J.R. Yates, L.G. Ciffo, S. Patsias
Dynamic crushing of auxetic open-cell polyurethane foam
Proc Inst Mech Eng Part C, 216 (12) (2002), pp. 1153-1156, 10.1243/095440602321029382
- [9] L.L. Hu, M.Z. Zhou, H. Deng
Dynamic indentation of auxetic and non-auxetic honeycombs under large deformation
Compos Struct, 207 (2019), pp. 323-330, 10.1016/j.compstruct.2018.09.066
- [10] N. Novak, L. Starčević, M. Vesenjaj, Z. Ren
Blast response study of the sandwich composite panels with 3D chiral auxetic core
Compos Struct, 210 (2019), pp. 167-178, 10.1016/j.compstruct.2018.11.050
- [11] C. Qi, A. Remennikov, L.Z. Pei, S. Yang, Z.H. Yu, T.D. Ngo
Impact and close-in blast response of auxetic honeycomb-cored sandwich panels: experimental tests and numerical simulations
Compos Struct, 180 (2017), pp. 161-178, 10.1016/j.compstruct.2017.08.020
- [12] H. Wang, Z. Lu, Z. Yang, X. Li
A novel re-entrant auxetic honeycomb with enhanced in-plane impact resistance
Compos Struct, 208 (2019), pp. 758-770, 10.1016/j.compstruct.2018.10.024
- [13] A. Tsouknidas, M. Pantazopoulos, I. Katsoulis, D. Fasnakis, S. Maropoulos, N. Michailidis
Impact absorption capacity of 3D-printed components fabricated by fused deposition modelling
Mater Des, 102 (2016), pp. 41-44, 10.1016/j.matdes.2016.03.154
- [14] D.A. Debeau, C.C. Seepersad, M.R. Haberman
Impact behavior of negative stiffness honeycomb materials
J Mater Res, 33 (2018), pp. 290-299, 10.1557/jmr.2018.7
- [15] S. Hou, T. Li, Z. Jia, L. Wang
Mechanical properties of sandwich composites with 3d-printed auxetic and non-auxetic lattice cores under low velocity impact
Mater Des, 160 (2018), pp. 1305-1321, 10.1016/j.matdes.2018.11.002
- [16] G. Imbalzano, S. Linforth, T.D. Ngo, P.V.S. Lee, P. Tran
Blast resistance of auxetic and honeycomb sandwich panels: Comparisons and parametric designs
Compos Struct, 183 (2018), pp. 242-261, 10.1016/j.compstruct.2017.03.018
- [17] Y.T. Kao, A.R. Amin, N. Payne, J. Wang, B.L. Tai
Low-velocity impact response of 3D-printed lattice structure with foam reinforcement
Compos Struct, 192 (2018), pp. 93-100, 10.1016/j.compstruct.2018.02.042
- [18] Y. Jiang, Y. Li
3D printed auxetic mechanical metamaterial with chiral cells and re-entrant cores
Sci Rep, 8 (2018), pp. 1-11, 10.1038/s41598-018-20795-2
- [19] H.Y. Sarvestani, A.H. Akbarzadeh, H. Niknam, K. Hermenean
3D printed architected polymeric sandwich panels: Energy absorption and structural performance
Compos Struct, 200 (2018), pp. 886-909, 10.1016/j.compstruct.2018.04.002

- [20] H.Y. Sarvestani, A.H. Akbarzadeh, A. Mirbolghasemi, K. Hermenean
3D printed meta-sandwich structures: Failure mechanism, energy absorption and multi-hit capability
Mater Des, 160 (2018), pp. 179-193, 10.1016/j.matdes.2018.08.061
- [21] H.B. Rebelo, D. Lecompte, C. Cismasiu, A. Jonet, B. Belkassam, A. Maazoun
Experimental and numerical investigation on 3D printed PLA sacrificial honeycomb cladding
Int J Impact Eng, 131 (2019), pp. 162-173, 10.1016/j.ijimpeng.2019.05.013
- [22] Z. Vangelatos, G.X. Gu, C.P. Grigoropoulos
Architected metamaterials with tailored 3D buckling mechanisms at the microscale
Extr Mech Lett, 33 (2019), Article 100580, 10.1016/j.eml.2019.100580
- [23] G. Dolzyk, S. Jung
Tensile and fatigue analysis of 3d-printed polyethylene terephthalate glycol
J Fail Anal Prev, 19 (2019), pp. 511-518
- [24] S. Guessasma, et al.
Printability and tensile performance of 3d printed polyethylene terephthalate glycol using fused deposition modelling
Polymers, 11 (7) (2019), p. 1220
- [25] Guangyong Sun, et al.
Comparative study on aluminum/GFRP/CFRP tubes for oblique lateral crushing
Thin-Walled Struct, 152 (2020)
- [26] W. He, J. Liu, S. Wang, D. Xie
Low-velocity impact response and post-impact flexural behaviour of composite sandwich structures with corrugated cores
Compos Struct, 189 (2018), pp. 37-53
- [27] Wentao He, Shaojia Lu, Ke Yi, Shuqing Wang, Guangyong Sun, Zhiqiang Hu. Residual flexural properties of CFRP sandwich structures with aluminum honeycomb cores after low-velocity impact. *Int J Mech Sci* 2019;161–162: 2019.
- [28] Shunfeng Li, Xiao Guo, Jiapeng Liao, Qing Li, Guangyong Sun
Crushing analysis and design optimization for foam-filled aluminum/CFRP hybrid tube against transverse impact
Compos Part B, 196 (2020)
- [29] Lu. Yao, Guangyong Sun, Wentao He, Xiangjian Meng, De Xie
Investigation on impact behavior of FMLs under multiple impacts with the same total energy: Experimental characterization and numerical simulation
Compos Struct, 226 (2019), Article 111218
- [30] Guohua Zhu, Guangyong Sun, Yu. Hang, Shunfeng Li
Qing Li, Energy absorption of metal, composite and metal/composite hybrid structures under oblique crushing loading
Int J Mech Sci (2017)
- [31] Prusa Research S.R.O. "<https://www.prusa3d.com/>".
- [32] ASTM D638-14. Standard test method for tensile properties of plastics. Technical Report. West Conshohocken, PA; 2014.

- [33] Hugo Miguel Bento Rebelo. PhD Thesis, Development and study of a high performance protective solution against blast loads. UNL-FCT; 2020.
- [34] Silva A, Guilhon D. Comparative analysis of ankle prosthesis connector adapters in 3d printed using PLA and PETG. In: Costa-Felix R, Machado J, Alvarenga A, editors. XXVI Brazilian congress on biomedical engineering. IFMBE Proceedings, vol 70/1. Springer, Singapore; 2019.
- [35] L.S. Sutherland, C.G. Soares
The use of quasi-static testing to obtain the low-velocity impact damage resistance of marine GRP laminates
Compos Part B, 43 (2012), pp. 1459-1467, 10.1016/j.compositesb.2012.01.002
- [36] M. Garrido, R. Teixeira, J.R. Correia, L.S. Sutherland
Quasi-static indentation and impact in glass-fibre reinforced polymer sandwich panels for civil and ocean engineering applications
J Sandwich Struct Mater, 1099636219830134 (2019), 10.1177/1099636219830134
- [37] D.F. Meaney, B. Morrison, C. Dale Bass
The mechanics of traumatic brain injury: a review of what we know and what we need to know for reducing its societal burden
J Biomech Eng, 136 (2) (2014), 10.1115/1.4026364